CONF-9510111--5

ANL/ET/CP--90247

RECEIVED
SEP 0 3 1996
OSTI

Title: Thermal Diffusivity Imaging of Continuous Fiber Ceramic Composite Materials and Components

Authors: S. Ahuja, W. A. Ellingson, J. S. Steckenrider,† and S. King

Energy Technology Division, Argonne National Laboratory
9700 South Cass Ave., Argonne, IL 60439

†Northwestern University, Evanston IL 60208

The submitted manuscript has been authored by a contractor of the U. S. Government under contract No. W-31-109-ENG-38. Accordingly, the U. S. Government retains a nonexclusive, royalty-free license to publish or reproduce the published form of this contribution, or allow others to do so, for U. S. Government purposes.

MASTER

PROCESSED FROM BEST AVAILABLE COPY

DISCLAIMER

Portions of this document may be illegible in electronic image products. Images are produced from the best available original document.

ABSTRACT

Continuous-fiber ceramic matrix composites (CFCCs) are currently being developed for various high-temperature applications, including use in advanced turbine engines. In such composites, the condition of the interfaces between the fibers and matrix or between laminae in a two-dimensional weave lay-up are critical to the mechanical and thermal behavior of the component. A nondestructive evaluation method that could be used to assess the interface condition and/or detect other "defects" has been developed at Argonne National Laboratory (ANL) and uses infrared thermal imaging to provide "single-shot" full-field quantitative measurement of the distribution of thermal diffusivity in large components. By applying digital filtering, interpolation, and least-squares-estimation techniques for noise reduction, shorter acquisition and analysis times have been achieved with submillimeter spatial resolution for materials with a wide range of "thermal thicknesses". The system at ANL has been used to examine the effects of thermal shock, oxidation treatment, density variations, and variations in fiber coating in a full array of test specimens. In addition, actual subscale CFCC components of nonplanar geometries have been inspected for manufacturing-induced variations in thermal properties.

INTRODUCTION

Advanced ceramics that meet the requirements of tomorrow's technology are currently being introduced into the manufacturing community. For example, the titanium alloy with a silicon carbide (SiC)-reinforced ceramic-matrix, Timetal-21S (Ti-15Mo-3Nb-3Al-0.2Si) has reduced the weight of each of the engines of the Boeing 777 by 360 kg. These materials, in general, have high strength and stability at high temperatures due to the incorporation of continuous fibers in monolithic ceramics. CFCCs are being considered as replacements for traditional materials in numerous applications, including gas turbines, due to their relatively high strength and toughness at high temperatures (>1250°C), and lower density. Among the specific materials systems under consideration are $SiC_{(f)}/SiC$ and $Al_2O_{3(f)}/Al_2O_3$, which are desired specifically for their thermal properties (i.e., thermal diffusivity, thermal conductivity, etc.) and therefore any variations in those properties will significantly affect their ability to transfer heat properly. Such variations result from processing defects, thermal shock, or thermally induced degradation of the fiber/matrix interface and reduce the advantages for choosing these materials.

Several nondestructive methods for the detection of thermal properties have been employed in the study of both ceramic and nonceramic materials systems [1]. These

methods are primarily utilized for specimens whose thermal properties are assumed uniform [2-5]. The critical issue in most CFCC applications, however, is the distribution of thermal properties within a given component. In these situations, thermal infrared imaging methods, which are of greater utility, have been employed as a nondestructive testing method for CFCCs with the limitation that the test methods employed are either not portable or very expensive. CFCCs emit energy in different directions, parallel and perpendicular to the two dimensional weave. Transmissivity, the ratio of energy transmitted by the material to the incident energy, is used to determine the wavelength at which a body transmits infrared energy and is important in infrared detection.

Nondestructive techniques such as ultrasonic testing have limitations due to the requirement that the test specimen be submerged in water, while CT scanning is effective but cannot be portable and inexpensive. Presently, acoustic emission and resonance are being researched, but more time is needed in order to determine their workability as test methods. Thermographic techniques are full-field and simultaneously and independently measure thermal properties over a 2-D distribution of locations. Since the detection and thermal excitation required is accomplished radiometrically, the method is inherently noncontact and can be performed at elevated temperatures.

This paper describes a modified thermographic imaging technique to the measurement of thermal diffusivity of a number of SiC/SiC CFCC specimens and components. Currently, the available commercial equipment for infrared analysis limits the size of components to 10 to 15 mm diameter and 6 mm thickness requiring high spatial resolution and long acquisition times [6]. The approach of the experiment is to use a commercially available infrared camera, a suitable thermal excitation device, and locally written software to automate the entire test setup. Complete thermal history is recorded for the specimen area of interest from the time of thermal excitation until the surface reaches its maximum temperature. From this temperature-time relationship, thermal diffusivity is calculated by two methods. By imaging at a higher resolution than required and spatially averaging the resulting images before computation of the diffusivity, sufficient noise reduction is achieved in a single heating cycle while maintaining the required spatial resolution.

EXPERIMENTAL DETAILS

The thermal imaging system used for this work is illustrated in Fig. 1. This system uses the method of Parker et al. [7] to calculate thermal diffusivity requiring a thermal pulse of short duration to be incident upon the front surface of a specimen and the temperature of the back surface to be monitored as a function of time. This was accomplished by heating the front surface of the specimen using a 6 kJ photographic flash lamp with a pulse duration of less than 8 ms and monitoring the back-surface temperature using a commercially available scanning radiometer infrared camera. The camera was equipped with a 3-12 μm optical band-pass lens system and a liquid-nitrogen-cooled HgCdTe detector. Images were acquired using a Mac II with an on-board frame grabber capable of storing 128 images in real time at 512 x 512 pixel 8-bit resolution. The frame grabber board received standard RS-170 signals from the infrared camera and digitized each received image, which was then processed with locally developed software. The software extracted the average gray scale value representing the temperature of the specimen. Specimens were mounted in diatomaceous earth having low thermal conductivity and minimizing lateral heat flow. By determining the position of the scanning mirrors at the time of the flash (e.g., by determining which of the 512 image rows was excited by the flash) the exact flash time could be determined with sub-millisecond resolution.

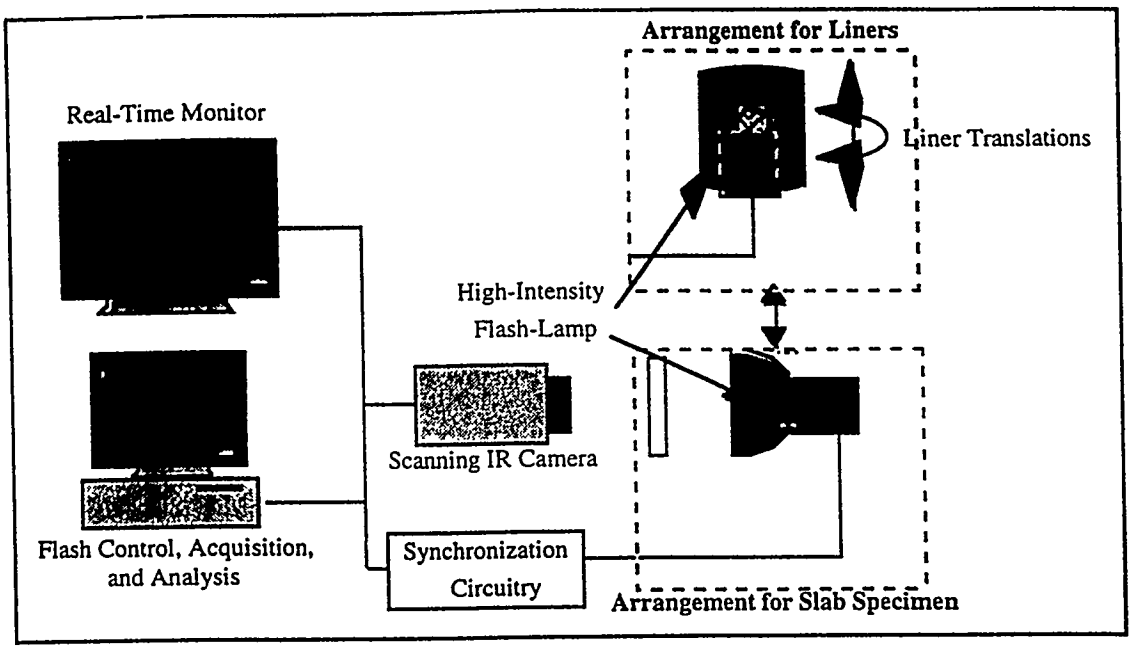

Figure 1: Diagram of experimental arrangement used for thermal diffusivity imaging.

Figure 2 shows the theoretically predicted back-surface temperature T as a function of time t and specimen thickness L according to Parker et al. [7] from the relationship

$$T(L,t)=\frac{Q}{\rho CL}\left[1+2\sum_{n=1}^{\infty}(-1)^n \exp\left(\frac{-n^2\pi^2}{L^2}\alpha t\right)\right], \qquad (1)$$

where Q is the radiant energy incident on the front surface, ρ is density, C is specific heat, and α is the thermal diffusivity. Because the axes of Fig. 2 have been normalized (where T_M is the maximum back surface temperature), it is universal to all specimens. Two methods of determining α from the graph become evident. First, the more common method notes that when V = 0.5 (the back-surface temperature rise has reached half of its maximum), $\omega = 1.37$. Thus, using the "half-rise time" method,

$$\alpha=\left(\frac{1.37\,L^2}{\pi^2 t_{\frac{1}{2}}}\right). \qquad (2)$$

As is evident from the plot of Fig. 2, any noise in the temperature signal can significantly alter the computed thermal diffusivity value. Because the noise level in scanning radiometers is notoriously high (as much as 10% for temperature variations on the order of a few degrees Celcius in the current system), some method of noise reduction must be performed. Previous researchers have performed a "cyclic averaging" procedure in which the specimen is heated and allowed to cool a number of times, and the time-temperature history for all such cycles is averaged [7]. They have also employed a nonlinear least squares estimation of the entire time-temperature relationship which requires significant computation time. To minimize the time necessary to measure thermal diffusivity, and because the curve is nearly linear in the immediate vicinity, a linear least squares fit was used to interpolate the value of $t_{1/2}$.

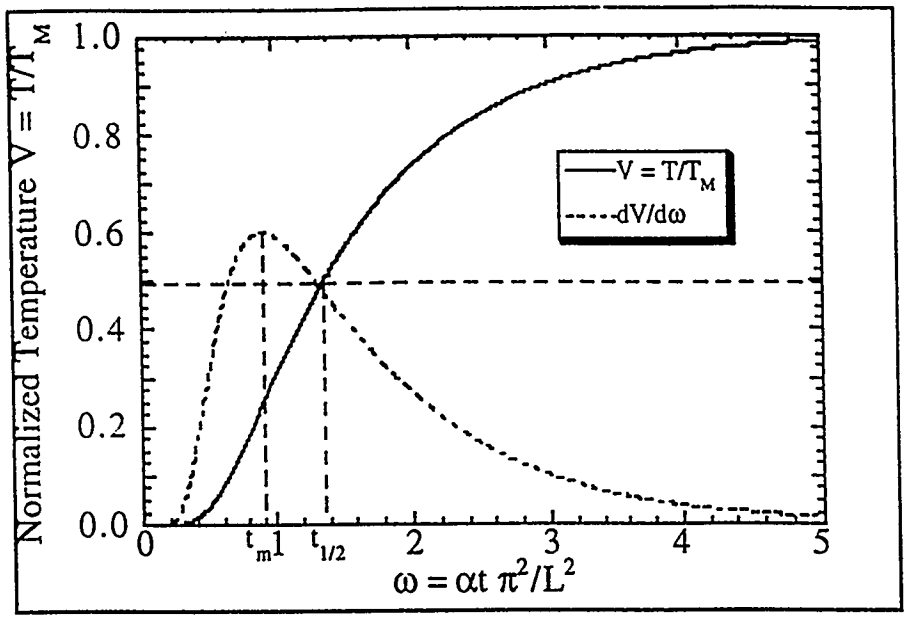

Figure 2. Theoretical plot of normalized back-surface temperature as a function of normalized time.

Furthermore, by imaging the components at higher resolution than required, spatial averaging, at a size which could be specified for the particular application, was permissible without loss of sensitivity to the minimum defect size. For the results presented here, a 10 x 10 pixel block was used. Thus a 512 x 413 pixel digitized image was transformed into a 51 x 41 pixel reduced image with a substantially better signal-to-noise ratio. As an additional means of noise reduction, the quarter-rise time ($t_{1/4}$) and three-quarter-rise time ($t_{3/4}$) were also determined for each block, where $\omega(t_{1/4}) = 0.92$ and $\omega(t_{3/4}) = 2.08$, according to the extension of Parker et al.'s procedure suggested in ASTM specification E 1461-92 [8]. The thermal diffusivity values obtained at these locations were averaged with that of the $t_{1/2}$ value to determine the effective thermal diffusivity. This permitted the determination of thermal diffusivity from a single thermal cycle, thereby reducing the total acquisition time.

The resulting thermal diffusivity values for all 10 x 10 pixel subsets were assembled into diffusivity images and were stored with 16-bit resolution. This avoided the need to scale each image independently (for better comparison between images) while retaining flexibility for image enhancement in display (which was performed at 8-bit resolution) [9]. The system was further modified by incorporating an autotrigger circuit, developed locally, to repeatably fire the flash, giving a dependable time for the diffusivity calculations. This autotrigger circuit has eliminated the need to manually locate the frame of the flash thereby providing a more precise value of the flash-time. Another commercially available, fully integrated, self-contained infrared camera equipped with a 3-5 μm optical band-pass lens system and based on the second-generation focal plane technology was also utilized. The electronics of this camera allowed for user-selectable intensity transform algorithms for contrast enhancement of the output image. Nonuniformity correction was selected to eliminate the variations in pixels in the focal plane array. Automatic gain control dynamically optimized the video contrast and brightness on a frame-by-frame basis. providing additional resolution in the acquired images.

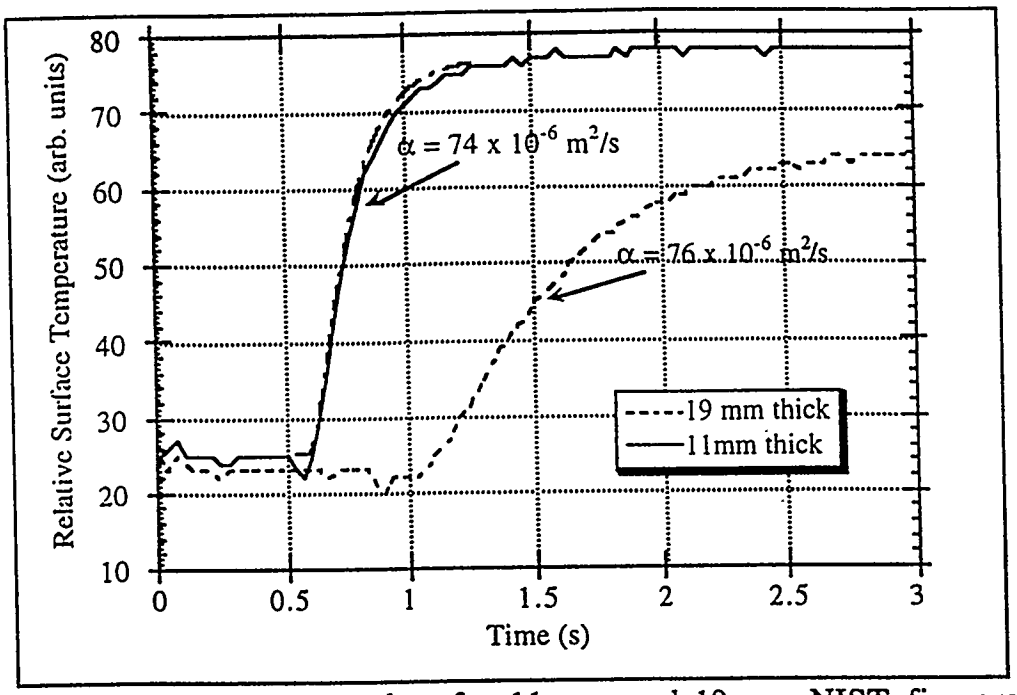

Figure 3. Time-temperature plots for 11 mm and 19 mm NIST fine-grained isotropic graphite specimens obtained with the half-rise-time thermal diffusivity system.

RESULTS

CALIBRATION SPECIMEN

Samples from the National Institute of Science and Technology (NIST) were used to determine the accuracy of the infrared image analysis system. The first specimens examined in this work were several thermal-property calibration standards (8426 graphite) with a stated thermal diffusivity value of 72 x 10^{-6} m^2/s. Three cylinders were cut from the 25.4-mm-diameter specimen provided with a diamond wafering saw in nominal thicknesses of 4, 11, and 19 mm. Figure 3 shows typical time-temperature plots for the 11 and 19 mm specimens, from which thermal diffusivity values of 74 and 76 x 10^{-6} m^2/s, respectively, were measured using the half-rise-time method and averaging over the center 1 cm^2. The resulting thermal diffusivity image for the 19 mm specimen is shown in Fig. 4. Despite the noise in the region surrounding the graphite disk, the thermal diffusivity clearly shows little variation across the face of the disk, indicating that the insulating mount was sufficient to ensure that lateral diffusion is indeed negligible over the time frame used to conduct these measurements. Furthermore, the standard deviation of thermal diffusivities measured in 1 cm^2 at the disk center was ± 2 x 10^{-6} m^2/s. Thus, the absolute value of the thermal diffusivity measured using this system deviated from the calibration value by ≈ 5% or less (owing to thermal losses and approximations in the determination of $t_{1/2}$), and the variation of that measured diffusivity was less than 3%.

SEEDED-DEFECTS SPECIMEN

The applications of the thermal diffusivity imaging system are primarily of interest in materials characterization. While they use the full-field nature of the technique, they are interested only in a single measurement from a given specimen, and therefore do

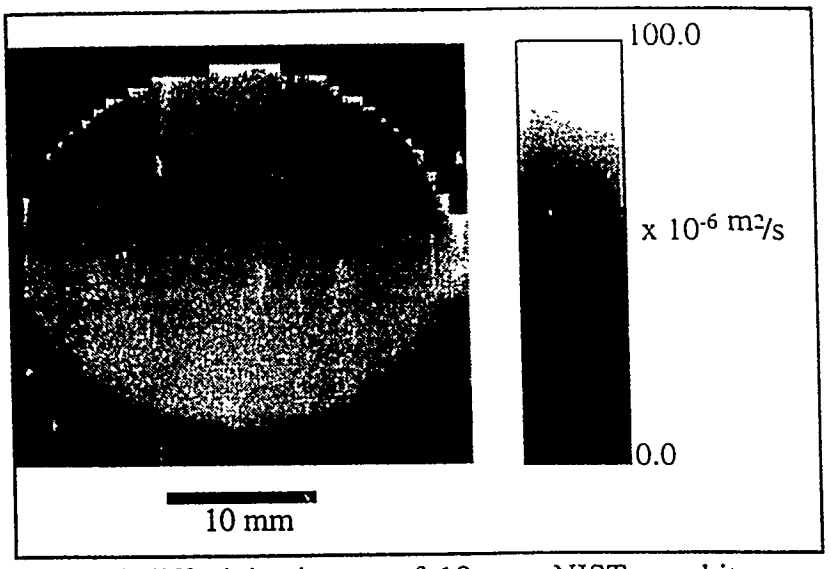

Figure 4. Thermal diffusivity image of 19 mm NIST graphite specimen, with absolute diffusivity scale shown at right.

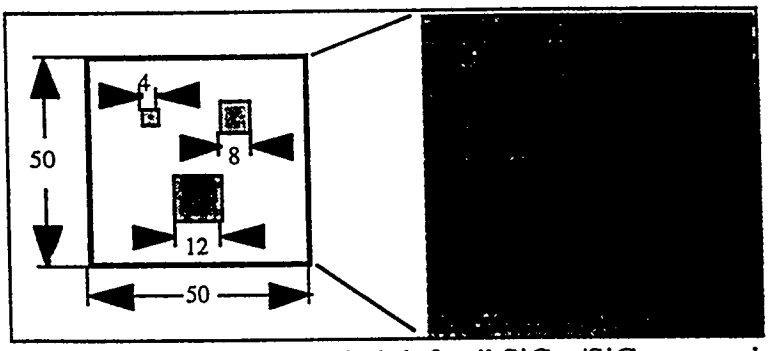

Figure 5. Schematic diagram of "seeded defect" $SiC_{(f)}/SiC$ composite panels used for defect detection (dimensions in mm) and X-ray radiograph.

not take full advantage of the system's capability to determine the distribution of thermal diffusivities. When examining actual components, the distribution of properties becomes critical, because what constitutes a potentially dangerous defect in one location might be an acceptable variation in another less hazardous location. To examine the system's capability to distinguish defects of various sizes in a $SiC_{(f)}/SiC$ CFCC, several "seeded-defect" $SiC_{(f)}/SiC$ composite panels were made. A total of 32 panels were created by varying several parameters (including graphoil section thicknesses, defects sizes, fiber coatings, defect depth, and infiltration density), and a diagram of one of these panels is shown in Fig. 5. The panels were made from 12 layers of 2-D plain weave Nicalon fabric. The simulated defects were created by cutting out small sections of two inner plies and replacing the fabric with graphoil sections. The weave was then infiltrated with SiC by CVI. Figure 5 also shows X-ray radiograph of the specimen indicating the defect locations. Figure 6 shows a comparison of the images generated for the $SiC_{(f)}/SiC$ panel. Figure 6a is the raw thermal images taken at the point of maximum thermal contrast between the defect and non-defect regions, and Fig. 6b is the same image after substantial image processing. While the defects are clearly evident in the processed image, the relative extent of "damage" is still unknown, and the image processing has required the interaction of a trained user. Furthermore, direct quantitative comparison of the two

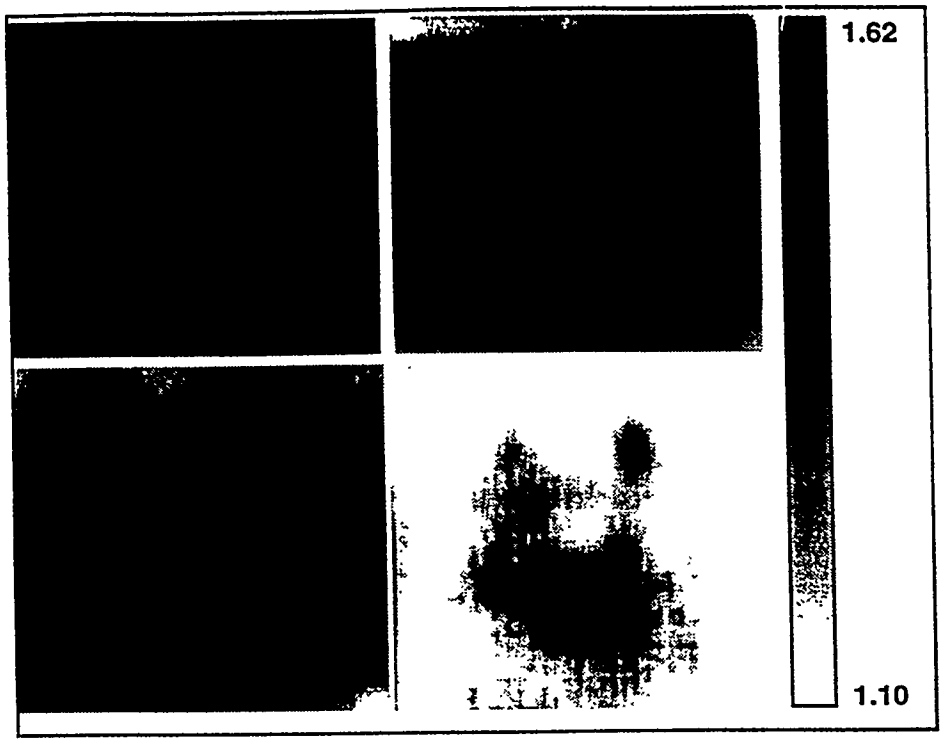

Figure 6. Images of a $SiC_{(f)}/SiC$ composite panels. Image (a) is the raw thermal image, (b) is the processed thermal image, (c) is the thermal diffusivity image and (d) is the thermal diffusivity image with second generation focal plane technology and user-selectable intensity transform algorithms for contrast enhancement of the output image (absolute diffusivity scales shown at right).

images is difficult at best. Figure 6c is the thermal diffusivity image of the specimen. Not only is the contrast as good as or better than the processed thermal images, but the spatial resolution is slightly better and no user interaction was required. Since the thermal diffusivity images are quantitative, direct comparison is possible not only between the defect and nondefect regions, in which the defect region has a higher diffusivity, but between the two porosities as well. Figure 6d was acquired by user-selectable intensity transform algorithms for contrast enhancement of the output image: gain control was dynamically adjusted to optimize video contrast and brightness on a frame-by-frame basis, providing additional resolution in the acquired image.

COMBUSTOR LINERS AND BURST RINGS

Infrared imaging techniques were applied to a combustor liner and two burst rings. Figure 7 shows photographs of the representative combustor liners and the burst rings, respectively, that have been used for thermal diffusivity mapping. A typical burst ring had an approximate circumference of 64 cm, a diameter of 20 cm, and a thickness of 3 mm. To reduce the effects of angular emissivity variation from the cylindrical surface, 12 sections (each approximately 5.0 x 5.0 cm) of the burst rings were imaged. The combuster liner had an approximate circumference of 64 cm, a diameter of 20 cm, and a thickness of 3 mm. Eleven sections per row of approximately 5.0 x 6.5 cm were imaged, and the overall height of the map from top to bottom was 15 cm.

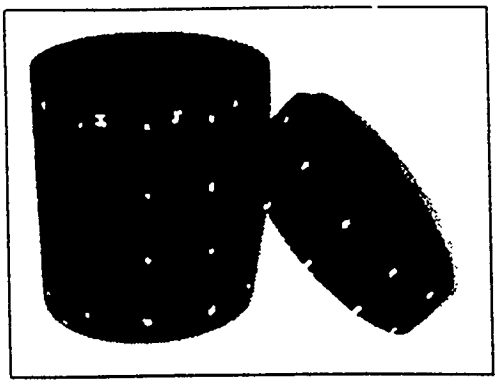

Figure 7. Photograph of combustor liner and burst ring.

The experimental configuration for the combustor liners and burst rings, as shown in Fig. 1. was modified in that the flash lamp was placed inside the liner while the IR camera monitored the temperature of the outside surface. Light from the flash lamp was concentrated by using aluminum foil inside the liner in an area (≈100 mm square) centered on but slightly larger than the segment of interest to prevent excessive lateral thermal diffusion from the region of interest. By containing the area exposed to the flash, the entire liner was not heated during each flash cycle. Thus, consecutive acquisitions of time-temperature profiles for nonadjacent segments were possible without allowing for the previously irradiated surface to cool completely, thereby minimizing overall acquisition time.

Figures 8 and 9 show the diffusivity maps for the burst rings along with the ultrasound testing maps which were available only for the burst rings. A direct correlation is observed in the maps in the identification of the voids, the point "A" being the orientation point of both the maps.

Thermal diffusivity images for the individual segments of the combustor liner were assembled into a single conformally mapped image as shown in Fig. 10a. The lines between segments are caused by tape used to mark their location. One large area of low thermal diffusivity is seen on the left side of the image, while other areas of higher diffusivity are seen as vertical bands across the image. The bands of higher diffusivity correlated well to the locations of seams in the weave lay-up. However,

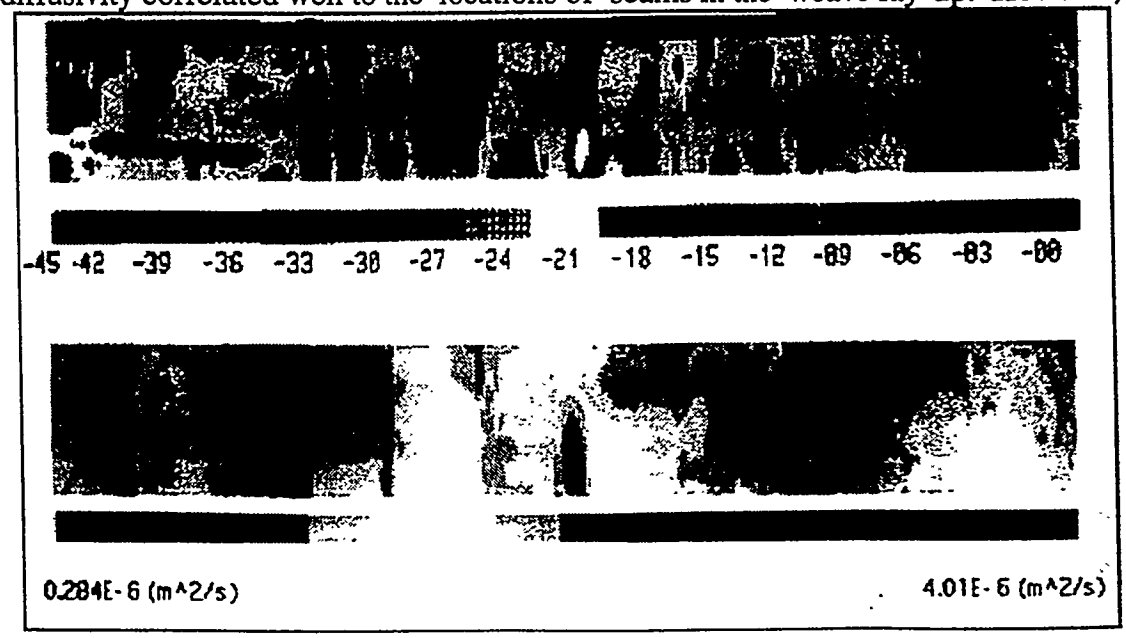

Figure 8: Top: Ultrasonic testing map. Bottom: IR imaging map for burst ring.

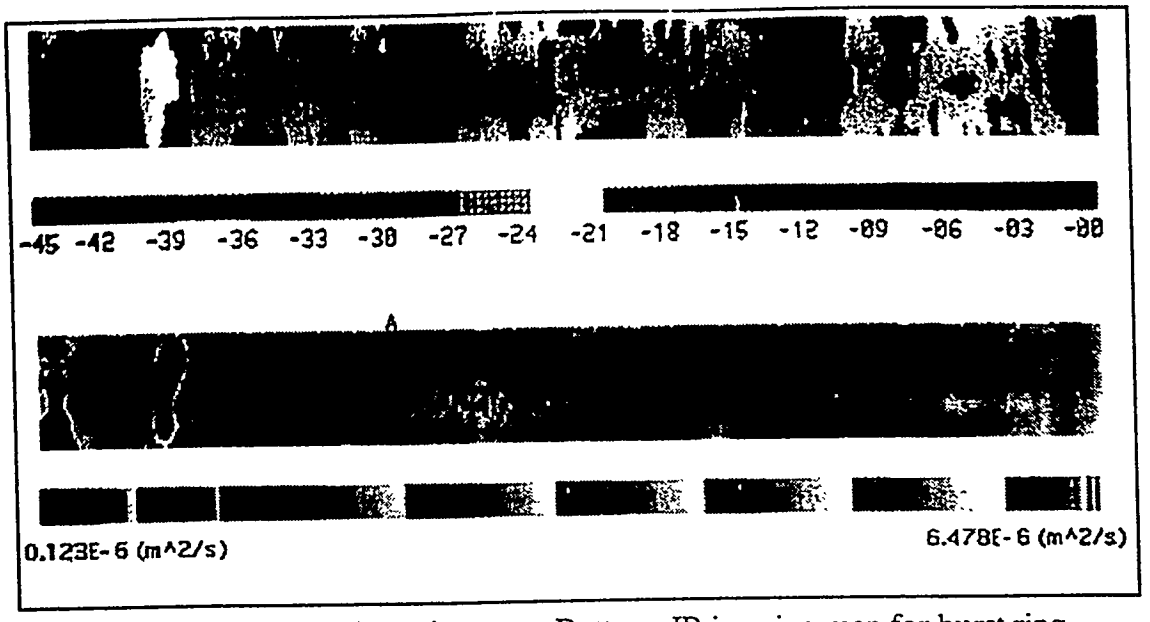

Figure 9: Top: Ultrasonic testing map; Bottom: IR imaging map for burst ring.

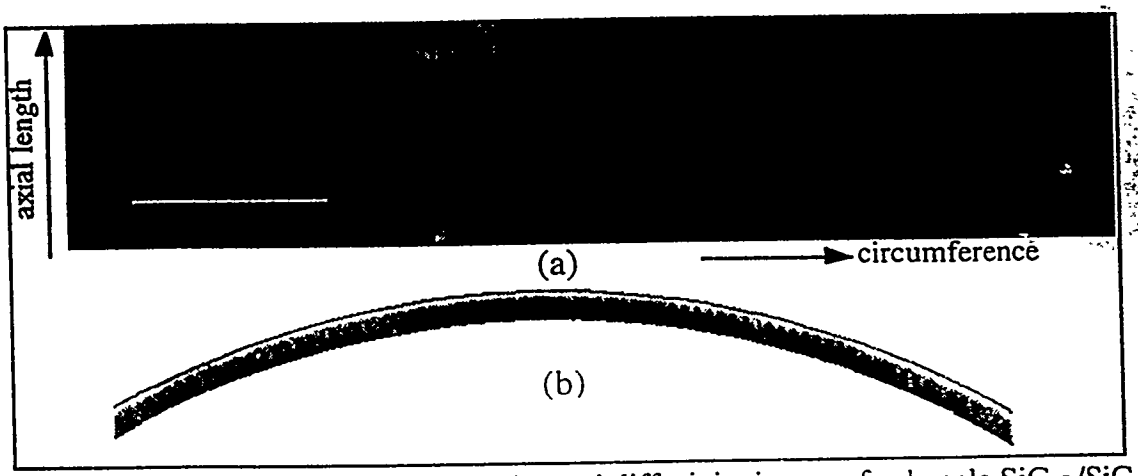

Figure 10. (a) Conformally mapped thermal diffusivity image of subscale $SiC_{(f)}/SiC$ combustor liner (where white = high diffusivity, black = low diffusivity) and (b) X-ray CT cross-section of same liner (where white = high density, black = low density) from location noted in (a).

the large region of low diffusivity was not related to any known geometrical condition of the liner. A density cross-section was therefore obtained for that region (as indicated in the figure) using a microfocus X-ray CT system, and this image is shown in Fig. 10b. Clearly, the region of low thermal diffusivity correlated directly to a region of low density (high porosity) in the liner, the result of poor matrix infiltration.

SiC/SiC COMPOSITE PANEL

A diffusivity map was acquired of a 4 x 4 in. 3D composite panel of SiC/SiC with angle interlock defects in specific locations shown in Fig. The through thicknesses and the weave row sketched in Fig. 12b are easily detected on the overall

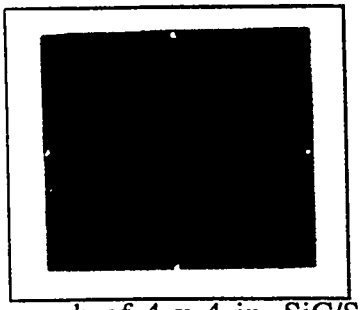

Figure 11. Digitized photograph of 4 x 4 in. SiC/SiC ceramic composite with special carbon fibers at selected locations. Bottom half of the photograph shows the interweave.

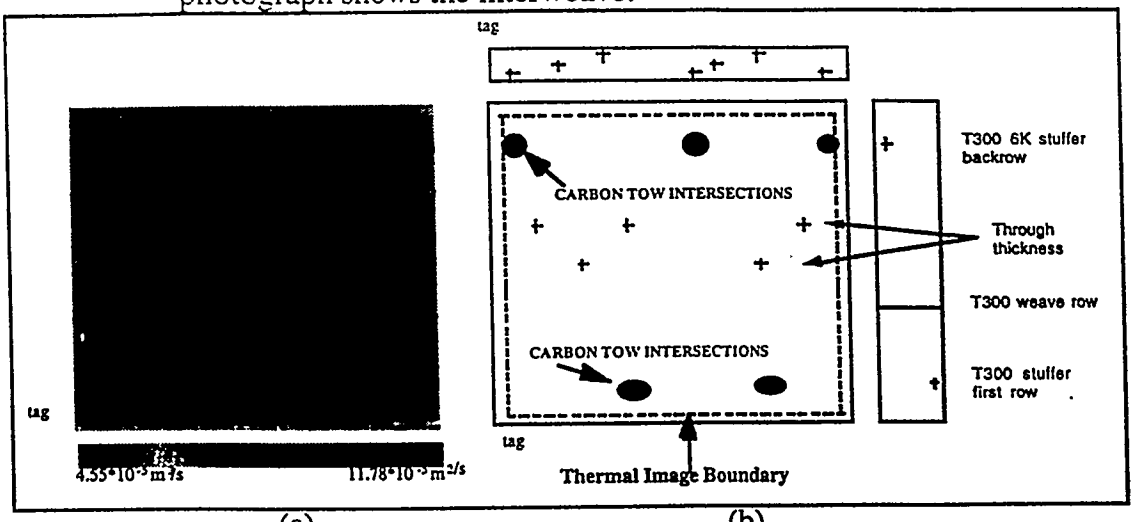

Figure 12. (a) Thermal diffusivity image showing foreign fiber detection (b) schematic diagram of 3-D weave SiC/SiC specimen showing locations of carbon tows.

diffusivity map of the panel shown in Fig. 12a. Data acquisition was conducted by dividing the panel in four sections, scanning, and obtaining four diffusivity maps.

CONCLUSIONS

A full-field thermal-imaging-based nondestructive characterization method has been developed and is applicable to a wide variety of large continuous fiber ceramic components. The data obtained by the thermal imaging nondestructive evaluation method have been correlated to delaminations, density variations, and other nondestructive evaluation methods. By applying digital filtering, interpolation, and least-square-estimation techniques for noise reduction, acquisition and analysis times of minutes or less have been achieved with submillimeter spatial resolution. In the future, sensitivity of full-field thermal diffusivity imaging will be enhanced, fatigue damage will be correlated, and methods will be investigated to allow measurement of diffusivity at higher temperatures.

ACKNOWLEDGMENTS

The authors would like to acknowledge the funding granted them by the U.S. Department of Energy, Energy Efficiency and Renewable Energy, Office of Industrial Technologies, under Contract W-31-109-ENG-88.

REFERENCES

1. J. S. Steckenrider, W. A. Ellingson and S. A. Rothermel, "Full-Field Characterization of Thermal Diffusivity on Continuous-Fiber Ceramic Composite Materials and Components", *Thermosense XVII: An International Conference on Thermal Sensing and Imaging Diagnostic Applications*, SPIE Proceedings Vol. 2473, S. Semanovich, Ed., Bellingham, WA, 1994.

2. F. Enguehard, D. Boscher, A. Déom and D. Balageas, "Measurement of the thermal radial diffusivity of anisotropic materials by the converging thermal wave technique," *Mat. Sci. Eng.*, Vol. B5 (2), pp. 127-134 (1990).

3. A. Hafidi, M. Billy and J. P. Lecompte, "Influence of microstructural parameters on thermal diffusivity of aluminium nitride-based ceramics," *J. Mat. Sci.*, Vol. 27 (12), pp. 3405-3408 (1992).

4. J. Rantala, L. Wei, P. K. Kuo, J. Jaarinen, M. Luukkala and R. L. Thomas, "Determination of thermal diffusivity of low-diffusivity materials using the mirage method with multiparameter fitting," *J. Appl. Phys.*, Vol. 73 (6), pp. 2714-2723 (1993).

5. I. Hatta, "Thermal diffusivity measurements of thin films and multilayered composites," Int. J. Thermophysics, Vol. 9 (2), pp. 293-303 (1990).

6. K. E. Cramer, W. P. Winfree, E. R. Generazio, R. Bhatt and D. S. Fox, "The application of thermal diffusivity imaging to SiC fiber reinforced silicon nitride," in Review of Progress in Quantitative Nondestructive Evaluation, D. O. Thompson and D. E. Chimenti, eds., Vol. 12, p. 1305, Plenum, New York (1993).

7. W. J. Parker, R. J. Jenkins, C. P. Butler and G. L. Abbott, "Flash method of determining thermal diffusivity, heat capacity, and thermal conductivity," *J. Appl. Phys.*, Vol. 32 (9), pp. 1679-1684 (1961).

8. American Society for Testing and Materials, "Standard test method for thermal diffusivity of solids by the flash method," Annual Book of ASTM Standards, ASTM E 1461-92 (1992).

9. W. A. Ellingson, S. A. Rothermel, J. F. Simpson, "Nondestructive Characterization of Ceramic Composites used as Combustor Liners in Advanced Gas Turbines", *Trans. ASME*, 95-GT-404, American Society of Mechanical Engineers, New York, NY (1995).

10. A. Sala, Radiant Properties of Materials - Tables of Radiant Values for Black Body and Real Materials. Elsevier Science Publishing Co. Inc., New York, 1986.

11. W. R. Barron, "The Principles of Infrared Thermometry", Sensors. December, 1992.